Tailoring exchange couplings in magnetic topological-insulator/antiferromagnet heterostructures

Qing Lin He[1][★][†], Xufeng Kou[1][†], Alexander J. Grutter[2][†], Gen Yin[1][†], Lei Pan[1], Xiaoyu Che[1], Yuxiang Liu[1], Tianxiao Nie[1], Bin Zhang[3], Steven M. Disseler[2], Brian J. Kirby[2], William Ratcliff II[2], Qiming Shao[1], Koichi Murata[1], Xiaodan Zhu[1], Guoqiang Yu[1], Yabin Fan[1], Mohammad Montazeri[1], Xiaodong Han[3], Julie A. Borchers[2] and Kang L. Wang[1][★]

Magnetic topological insulators such as Cr-doped (Bi,Sb)$_2$Te$_3$ provide a platform for the realization of versatile time-reversal symmetry-breaking physics. By constructing heterostructures exhibiting Néel order in an antiferromagnetic CrSb and ferromagnetic order in Cr-doped (Bi,Sb)$_2$Te$_3$, we realize emergent interfacial magnetic phenomena which can be tailored through artificial structural engineering. Through deliberate geometrical design of heterostructures and superlattices, we demonstrate the use of antiferromagnetic exchange coupling in manipulating the magnetic properties of magnetic topological insulators. Proximity effects are shown to induce an interfacial spin texture modulation and establish an effective long-range exchange coupling mediated by antiferromagnetism, which significantly enhances the magnetic ordering temperature in the superlattice. This work provides a new framework on integrating topological insulators with antiferromagnetic materials and unveils new avenues towards dissipationless topological antiferromagnetic spintronics.

In magnetic topological insulators (MTIs), time-reversal symmetry is broken and a gap is opened in the topological surface states by the ferromagnetic order, driving the metallic surface Dirac fermions into a massive state[1–3]. The presence of both topological surface bands and time-reversal symmetry breaking imbues the MTI with exotic physics, including the quantum anomalous Hall effect[3], axion electrodynamics[4], and spin–orbit torque[5]. Incorporating magnetic elements into TIs has been proved to be an effective approach to introduce ferromagnetism, as manifested by recent realizations[6–8] of the quantum anomalous Hall effect in Cr/V-doped (Bi,Sb)$_2$Te$_3$. The applicability of such an exotic effect can be greatly expanded by utilizing interfacial magnetic interactions to increase the Curie temperatures (T_C). For instance, it is proposed that when a TI is integrated with a ferromagnet (FM), proximity effects at the interface involving the surface Dirac fermions will align spin moments of the TI band with the itinerant carriers and give rise to ferromagnetism[2,9–12]. Since proximity effects occur locally at the interface, the ordering temperatures of the FM/TI heterostructure are primarily expected to be determined by the FM. Recent experimental observations suggest that the interplay between ferromagnetic EuS and the spin–orbit coupling in undoped TI thin film might enhance the magnetic order in both materials, and thus magnetize the TI surface layer near room temperature, due to the intricate interaction between the spins in Eu atoms and the TI surface states[13].

Similar proximity-induced surface state magnetization can also occur at the interface between TIs and antiferromagnets (AFMs). Although AFMs do not have macroscopic magnetization[13,14], in principle, short-range interfacial exchange coupling to an uncompensated AFM plane can locally magnetize the surface if an atomically sharp interface is achieved[15,16]. In this work we utilize

systematic doping and heterostructure engineering to demonstrate that such surface magnetization is not only possible at AFM/MTI interfaces, but that the magnetic properties of these systems can be greatly enhanced through such interfacial engineering. We show that, due to proximity effects, the Cr dopants in the MTI experience interfacial exchange coupling. This interfacial exchange coupling in the heterostructure tailors the spin texture in both the AFM and MTI layers, introducing an effective long-range exchange coupling between the MTI layers mediated by the AFM layers. Since this long-range exchange is induced by the antiferromagnetic order with a Néel temperature (T_N) up to ∼700 K, the ferromagnetic order and corresponding MTI transport signatures can survive at much higher temperatures compared to those of isolated MTI films (a factor of three increase of T_C). As a result, the AFM/MTI interfacial exchange coupling leads to a giant enhancement in the magnetic ordering. This modified spin texture is studied across wide variations in heterostructure thickness, periodicity and Cr-doping concentration.

The AFM CrSb (lattice constants $a = 4.122$ Å; ref. 14), is among the few antiferromagnetic materials lattice-matched with Cr-doped (Bi,Sb)$_2$Te$_3$MTI ($a = 4.262$–4.383 Å), making it an ideal candidate for the growth of epitaxial AFM/MTI heterostructures and superlattices (SLs) by molecular beam epitaxy (see Methods). The high crystal quality and extremely sharp interfaces of these two materials can be seen in the high-resolution transmission electron microscopy images shown in Fig. 1a, which is also confirmed by X-ray structural characterization (Supplementary Figs 1, 2, and Supplementary Information part (a)). The magnetic moments of the MTI layers exhibit strong perpendicular anisotropy regardless of layer thickness[7,8], while in bulk AFM CrSb the Cr spins lie along the
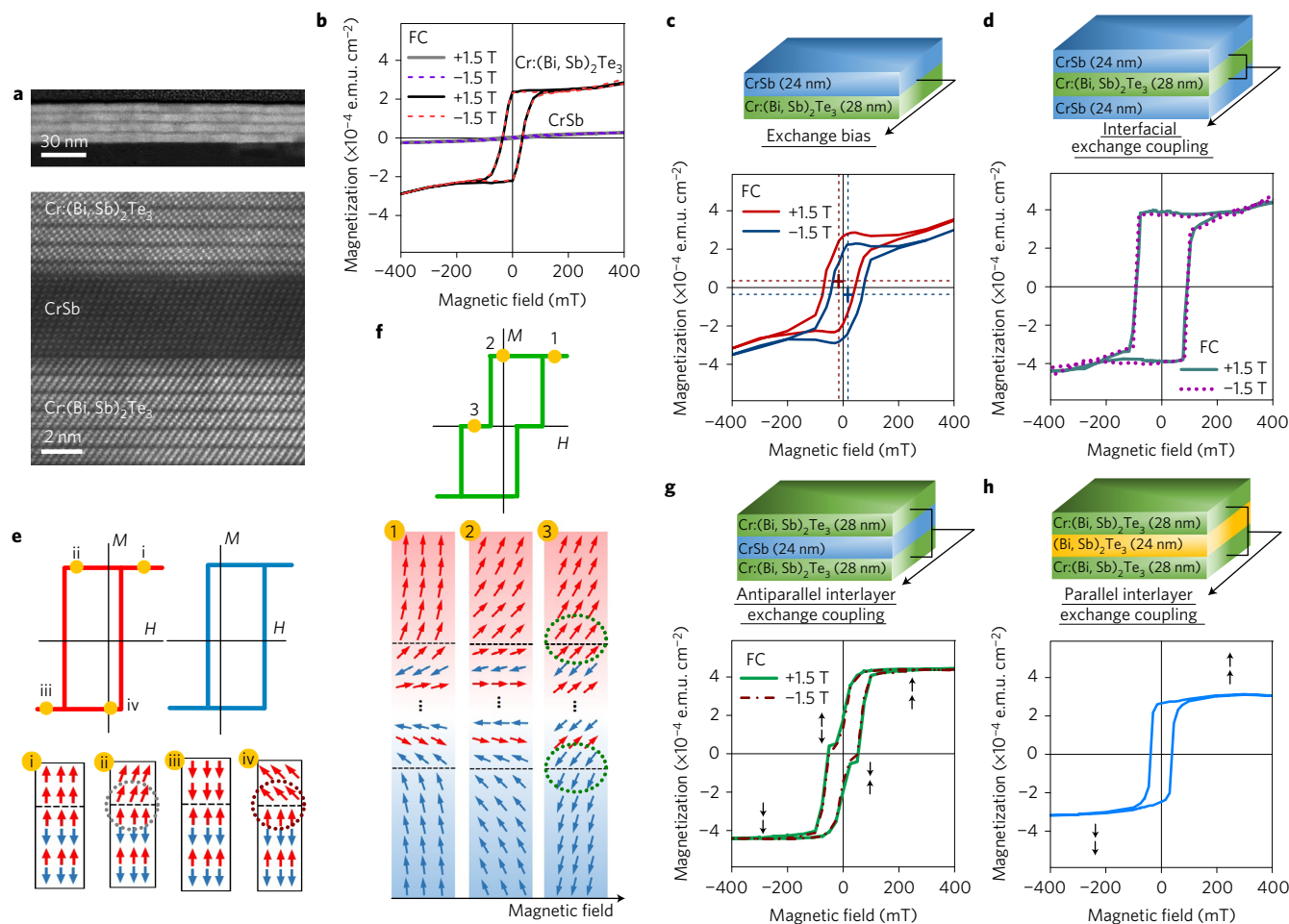
Figure 1 | Exchange couplings of Dirac fermions and AFM for different heterostructures. a, High-resolution transmission electron microscopy images of an AFM (CrSb)/MTI [Cr-doped $(Bi,Sb)_2Te_3$] superlattice. **b**, The perpendicular anisotropy of a MTI single layer is demonstrated by the square-shaped $M–H$ loops measured under a perpendicular magnetic field at 5 K, while the antiferromagnetic order of the AFM single layer is evidenced by the negligible net magnetization. **c**, Exchange bias observed in an AFM/MTI bilayer is demonstrated by the lateral shift (marked by dashed lines and crosses) of the $M–H$ loops (red and blue) under different perpendicular field-coolings. Cooling in a positive field results in a negative shift (red loop, −10.8 mT) and vice versa (blue loop, +11.0 mT). **d**, In an AFM/MTI/AFM trilayer, the two coupled AFM/MTI interfaces dramatically increase the coercive field of the MTI but eliminate the exchange bias due to the symmetry of the structure, whose effects from two surfaces are cancelled out. **e**, The schematic orientations of the atomic moments in the exchange-biased AFM/MTI bilayer, illustrating strong magnetic interactions between the MTI surface spins and the AFM spins. When the external field reverses the magnetization of the MTI, the AFM spins do not follow the field but try to keep the FM spins in their original orientations. Consequently the external field needed to reverse an exchange-biased MTI is larger than for a single MTI layer. **f**, The relative orientations of the atomic moments of the effective long-range exchange coupling in a MTI/AFM/MTI trilayer, which is generated from a LLG quantitative simulation and calculation using the saturation magnetization obtained from the PNR results, as described in Fig. 3. The interfacial exchange coupling between the Dirac fermions and the AFM spins orients the magnetization directions of the two MTI layers, forming a stable field-induced Néel-type domain wall within the AFM. **g**, A novel antiparallel effective long-range exchange coupling is observed in a MTI/AFM/MTI trilayer, which supports that this texture is mediated by the interactions between the MTI surface spins and AFM spins. **h**, A control trilayer that replaces the AFM layer in **g** by an undoped TI layer with the same thickness, which is nonmagnetic. In this system, the antiparallel effective long-range exchange coupling is eliminated; this result demonstrates the significant role of the exchange interactions between Dirac fermions and AFM spins for stabilizing the magnetic configuration.

c-axis, exhibiting A-type antiferromagnetic order with spins aligned ferromagnetically within the basal plane and antiferromagnetically between adjacent planes (T_N around 700 K; ref. 15). To achieve a highly insulating bulk character of the MTI layers, the Bi:Sb ratio is optimized to be 0.26:0.62 with various Cr-doping concentrations, positioning the Fermi level within the surface gap[8].

The perpendicular anisotropy of the MTI layer (28 nm, Cr-doping concentration $x = 0.16$), which is confirmed by the nearly square $M–H$ loop obtained under an applied perpendicular magnetic field (Fig. 1b), is essential for opening a surface gap and achieving the quantum anomalous Hall effect. In contrast, a negligible net magnetization is observed in the nominally AFM single layer (24 nm) of CrSb (Fig. 1b). In the bilayer AFM

(24 nm)/MTI (28 nm) (Fig. 1c), we observed an increase in the coercive field (H_C; ref. 16) to around 67 mT for the bilayer (as compared to around 47 mT for a MTI single layer) at 5 K. Such an increase is probably related to the exchange coupling between the MTI and the AFM spins at the interface, which is further evidenced by the interface sensitivity: on the one hand, by adding a second AFM layer (24 nm) at the bottom (that is, forming an AFM/MTI/AFM trilayer, Fig. 1d), H_C can be further enhanced to around 90 mT, given the fact that the number of the coupled interfaces is now doubled; on the other hand, the enhancement of H_C is found to be gradually reduced by increasing the thickness of the MTI layer (Supplementary Fig. 3), indicating surface-dominated ferromagnetism. Equally important, the exchange bias of the bilayer
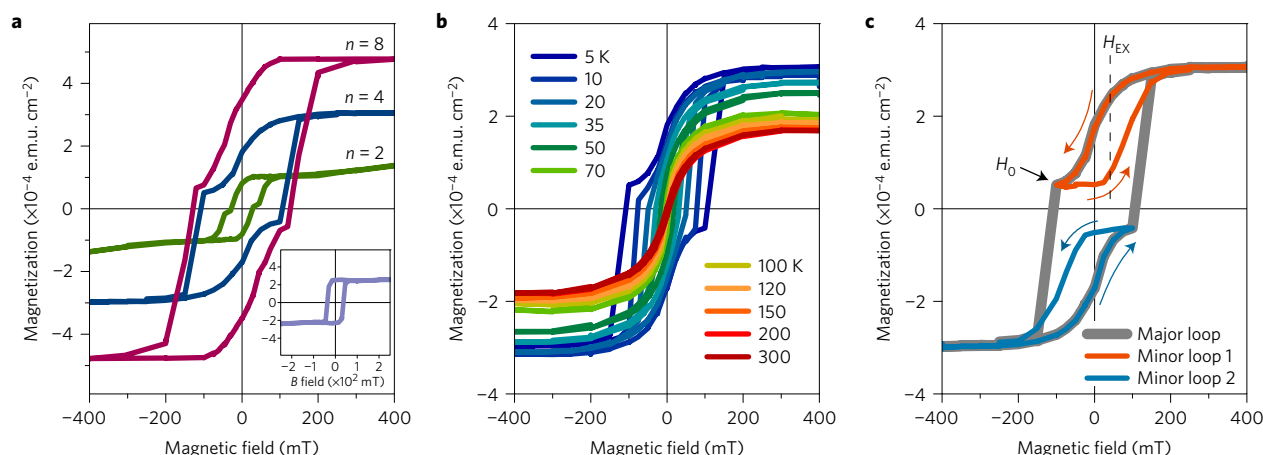
Figure 2 | Novel magnetic interplays in MTI/AFM superlattices (SLs). a, Antiparallel effective long-range exchange coupling in $(AFM/MTI)_n$ SLs with $n = 2$, 4 and 8, as demonstrated by the double-step behaviours in the M–H loops measured at 5 K. Similar to the trilayer in Fig. 1g, this behaviour is attributed to the antiparallel magnetizations between the neighbouring MTI layers in the SLs, which originates from the interactions between the MTI surface spins and AFM spins. The inset shows the magnetization of a control SL $(TI/MTI)_{n=4}$, in which the AFM layers are replaced by an undoped TI layer with the same thickness. In this case, the lack of exchange couplings between the Dirac fermions and AFM spins only contributes a single step switching behaviour. **b**, M–H loops showing that the double-step switching behaviour persists up to ~80 K, after which it becomes paramagnetic ($n = 4$). **c**, Exchange field H_{EX} between the neighbouring MTI layers in the SLs ($n = 4$) probed by minor loop measurements, as marked by the dashed line. These extracted H_{EX} values are used for the studies of temperature- and n-dependent exchange couplings in Fig. 4a,b. The grey loop indicates the major loop, while the red-orange and blue loops indicate the two minor loops. A typical minor loop 1(2) begins at $+(-)1.5$ T, decreases to $-(+)$ a specific value (H_0), then sweeps back to $+(-)1.5$ T; H_0 is a critical field value that is just above the onset of the second step switching.

resulting from coupling between the AFM spins and the surface spins of the MTI layer give rise to lateral negative and positive shifts of coercive fields under perpendicular field-cooling conditions, as observed in Fig. 1c and schematically illustrated by the red and blue curves in Fig. 1e, respectively[16]. The exchange bias persists up to around 35 K (Supplementary Fig. 4), slightly lower than T_C (around 38 K) of a single MTI layer, indicating that the biased magnetization originates within the MTI. In addition to the lateral exchange-biased shift, we also observed a characteristic vertical shift in magnetization, which may originate from uncompensated AFM spins at the interface[17]. On the other hand, exchange bias is not observed in the symmetric AFM/MTI/AFM trilayer sample (Fig. 1d). All of these observations are consistent with the picture of exchange bias originating from a unidirectional perpendicular anisotropy established at the AFM/MTI interface[16], which implies the presence of strong interfacial exchange coupling.

Strikingly, when the AFM layer is instead sandwiched between two MTI layers—that is, a MTI(28 nm)/AFM(24 nm)/MTI(28 nm) trilayer in Fig. 1f,g—a unique M–H loop and distinct magnetic interactions develop. In sharp contrast to the bilayer, such a trilayer shows a negligible exchange bias in the corresponding M–H loops with or without field-cooling treatments. Anomalous Hall resistances obtained from transport measurements are consistent with the M–H loops (Supplementary Fig. 5 and Supplementary Information part (b)). Instead, a symmetrical M–H loop with a double-switching feature arises, indicating an effective long-range exchange coupling between the MTI layers mediated by the AFM layer. The explanation of this double switching is shown schematically in Fig. 1f. The total energy of the spin texture is determined by the competition between the Zeeman energy and the exchange energy: $E_{tot} = E_Z + E_{EX}$. When a large external field is applied (point '1' in the M–H loop), assuming the two MTI layers are interfacing with different AFM spin sublattices, a vertical misalignment occurs in the AFM layer to minimize E_{tot}. Here, E_Z is minimized, since both MTI layers are aligned with the external field. On the other hand, E_{EX} is increased in the AFM layer due to the vertical misalignment. When the external field reduces to zero (point '2'), $E_Z = 0$. Interestingly, this misalignment in the AFM

layer can survive at zero field such that the surface spins in the MTI layers are tilted in opposite directions, as if an effective long-range AFM exchange coupling occurs between the MTI surface spins. By further applying a negative external field (point '3'), the increase in E_Z switches one MTI layer before the other. After this, the vertical misalignment vanishes, such that E_{EX} is lowered both in the AFM layer and at the interfaces (as shown by the dotted circles). This lowered E_{EX} compensates the increase in E_Z contributed from one of the MTI layers anti-aligned with the external field. As a result, this anti-aligned configuration becomes a metastable state. From this double-switching M–H loop, we conclude that the MTI/AFM/MTI interfacial exchange effectively induces a long-range antiparallel exchange between the MTI layers mediated by the AFM layer. Quantitative Landau–Lifshitz–Gilbert (LLG) quantitative simulations and calculations, which demonstrate the competing effects of E_{EX} and E_Z as discussed above, are provided in Supplementary Fig. 6 and Supplementary Information part (c). As a control sample, the same measurement was carried out in a MTI/TI/MTI trilayer (Fig. 1h), where a single square-shaped M–H loop suggests that the effective long-range exchange between MTI layers vanishes without the AFM layer. Note that the above discussion applies only to the case where the two MTI layers coincide with two different AFM sublattices. On the other hand, when they interface the AFM with the same sublattice, the double-switching feature vanishes (see Supplementary Information parts (d–e)).

To quantitatively investigate the interplay between the antiferromagnetic order and the MTI surface spins, we further expand our structural engineering by using building blocks of AFM(4 nm)/MTI(7 nm) to construct n-period SLs over a range of $n = 2$–10. The effective long-range exchange coupling, denoted by the symmetrical double-switching behaviours in the corresponding M–H loops, is even more pronounced in all these SLs (Fig. 2a). More importantly, such coupling persists to a temperature that is much higher than T_C of a single MTI layer. For example, the coercive field, H_C, of the $n = 4$ SL (Fig. 2b) increases to 70 K and the double switching is also enhanced to this temperature. At temperatures above 80 K, the double switching disappears and is replaced by a
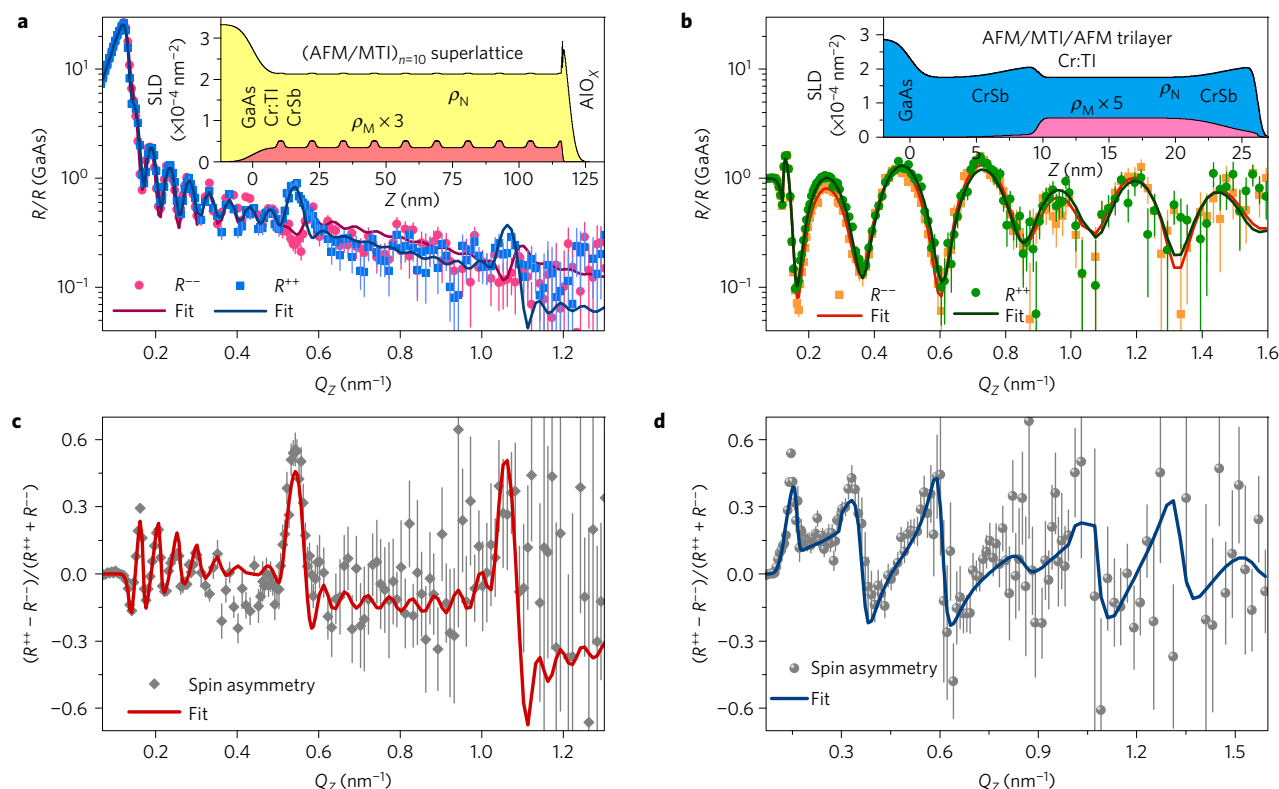
Figure 3 | Capturing the spin textures in the SL and trilayer by neutron techniques. a,b, Polarized neutron reflectivities (at 20 K with a 700 mT in-plane field) normalized to the GaAs substrates for the spin-polarized R^{++} and R^{--} channels of an $(AFM/MTI)_{n=10}$ SL (**a**) and an AFM/MTI/AFM trilayer (**b**). The insets show the corresponding models with structural and magnetic scattering length densities (SLDs), ρ_N and ρ_M, used to obtain the best fits, which contain magnetized TI and AFM layers for the SL, and a magnetized TI and two barely magnetized AFM layers for the trilayer. In the SL, the weak magnetization within the AFM layers is probably due to spin texture modification induced by proximity, consistent with the schematic shown in Fig. 1f. In contrast, in the trilayer the interaction between the MTI surface spins and the AFM spins at the interface dominates and the AFM texture remains almost intact. **c,d,** The detailed spin asymmetry $(R^{++} - R^{--})/(R^{++} + R^{--})$ between the R^{++} and R^{--} channels for the SL (**c**) and the trilayer (**d**). In **c**, only when both the MTI and AFM layers are magnetized can the spin splitting be well fitted, while the magnetization is assumed to be confined exclusively to the MTI layers or the AFM layers, that is, fails to describe the signs of spin splitting. In **d**, the best fit suggests that the AFM layer is barely magnetized (5 e.m.u. cm^{-3} or less, intrinsic AFM nature) while models assuming magnetized AFM layers fail to describe the spin asymmetry. The error bars are ±1 s.d.

paramagnetic response. Similar temperature dependences are also observed in SLs with $n = 2$, 6, 8, 10, confirming the giant T_C enhancement. Consistent with the MTI/AFM/MTI case discussed above, we also note that no signatures of exchange bias are observed in these SLs, again implying that the spin texture in the SL is different from that observed in the AFM/MTI bilayer. This suggests an AFM-mediated effective exchange coupling between the MTI layers in the SL similar to the MTI/AFM/MTI trilayer case.

To address the origin of such an effective long-range exchange coupling, we utilized polarized neutron reflectometry (PNR) to extract and compare the detailed temperature-dependent magnetization profiles of an $(AFM/MTI)_{n=10}$ SL and the AFM/MTI/AFM trilayer (see Methods)[18,19]. PNR was performed under an in-plane applied field of 700 mT to rotate the magnetization into the plane of the film. The fitted reflectivity of both the SL and trilayer, along with corresponding magnetic/structural depth profiles, are shown in Fig. 3. In the SL, we find net magnetizations of 47 and 62 e.m.u. cm^{-3} (1 e.m.u. cm^{-3} = 1 kA m^{-1}) on the MTI and AFM layers, respectively. Alternative models in which the net magnetizations are exclusively confined within either the MTI or AFM layers result in significantly worse fits to the data (Supplementary Fig. 7). It should be noted that, in modelling the SL, PNR spectra cannot distinguish well between uniform and modulated magnetization profiles (for example, Néel-type domain walls) within the AFM layers, and is consistent with a number of complex spin structures,

such as an oscillatory magnetization (Supplementary Fig. 7g). On the other hand, PNR of the trilayer shows a magnetization that is mostly confined to the MTI layers. Models which assume a magnetization of 62 e.m.u. cm^{-3} in the AFM layer fail to describe the data, while the best fit suggests a magnetization of 5 e.m.u. cm^{-3} or less (Supplementary Fig. 8 and Supplementary Information part (f)). At temperatures above T_C of the MTI, no net magnetization on either layer is observed. Thus, PNR results demonstrate that the AFM develops a net magnetization only when sandwiched between two MTI layers, whereby the spin texture is altered from the bulk.

Neutron diffraction measurements at zero applied field were further carried out on an $(AFM/MTI)_{n=15}$ SL to provide additional insight into the AFM spin structure (see Methods). The (0001) and (0002) hexagonal diffraction peaks are sensitive to the in-plane component of the AFM and FM structure, respectively, and were probed between 5 K and 300 K. Given that the net magnetization represents a small fraction of the total Cr moments even in an applied field of 700 mT, we expect minimal magnetic intensity at the (0002) peak location. Indeed, diffraction measurements show exclusively structural scattering at this location (Supplementary Fig. 9). Furthermore, the structural (0001) peak is forbidden in CrSb, and any scattering observed in this location must either be purely magnetic or originate in the MTI structure. However, no magnetic peak is observed, suggesting that the antiferromagnetically ordered
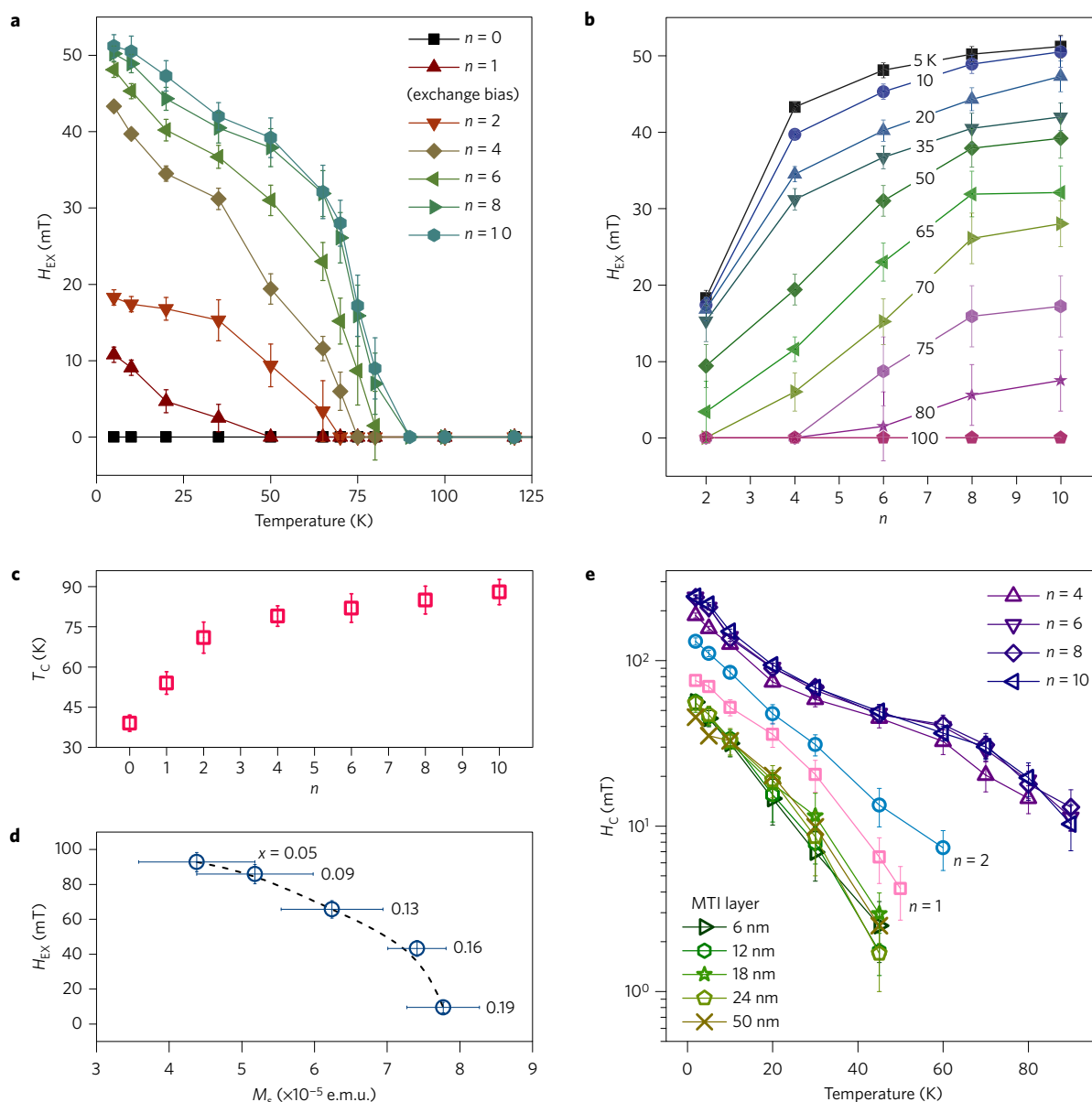
Figure 4 | Observation of giant enhancements in exchange field (H_{EX}), Curie temperature (T_C), and coercive field (H_C) in the superlattices.
a, Temperature-dependent H_{EX} obtained from $(AFM/MTI)_n$ SLs. It is noticed that H_{EX} persists at temperatures much higher than T_C of the MTI single layer, implying that the enhancement of magnetic ordering is strongly correlated with the effective long-range exchange coupling. **b**, H_{EX} isotherms as a function of n. **c**, T_C versus n. **d**, H_{EX} as a function of M_S, which corresponds to different Cr-doping concentrations (x) in five $(AFM/MTI)_{n=4}$ SLs, indicating the diminishing exchange coupling between the AFMs and the MTI surface spins. The decreases of H_{EX} along with the increasing M_S demonstrate the weakening of the effective long-range exchange coupling. The increase of the Cr-doping concentration makes the internal exchange energy large, and hence diminishes the double-switching signature, as indicated by the grey dashed line. **e**, H_C of MTI single layers and $(AFM/MTI)_n$ SLs versus T, showing H_C increases along with the increase of n, consistent with correlation between the effective long-range exchange coupling and magnetic ordering enhancement. The error bars specify the standard deviations of the measurements from the superconducting quantum interference device system.

spins in the CrSb layers may be oriented along the c-axis. In such an orientation, the magnetization is parallel to Q_z and the neutrons are not sensitive to this magnetic moment. Alternatively, it is possible that the antiferromagnetic order does not maintain phase coherence between AFM regions, resulting in magnetic peaks which are too broad to resolve. Combining the PNR and diffraction results, we conclude that the CrSb layers are magnetically ordered and that the spin structure is dramatically modulated from the bulk due to the effective long-range exchange coupling when sandwiched between two MTI layers (like the $(AFM/MTI)_n$ SLs and MTI/AFM/MTI cases). Consequently, the exchange bias is eliminated. In contrast, for an AFM layer in contact with a single MTI layer (like the

AFM/MTI bilayer case), the AFM spin texture remains mostly intact, and the exchange bias is preserved.

We find that magnetic ordering temperature is enhanced in the SLs, such that the transport signature of the magnetized Dirac fermions can survive at much higher temperatures compared to those observed in the isolated MTI thin films, as summarized in Fig. 4. In general, at the FM/AFM interfaces, the layer with a higher magnetic ordering temperature should enhance the ordering temperature of the interfacing material[20]. However, experimental demonstrations of an increase in T_C in the case of $T_N \gg T_C$ have been challenging, since a field-cooling process could not pin the antiferromagnetic order to avoid multi-domain effects[16,21,22]. In

our samples, the material quality of CrSb is carefully controlled such that multi-domain effects are minimized. At an atomically flat AFM/MTI interface, although the magnetization of the Dirac fermion surface states is dominated by the local spins of Cr dopants, the AFM/FM interfacial exchange pins the ferromagnetic order in the MTI layer, and thus supports the exchange gap of the massive Dirac fermions against temperature fluctuations. The presence of massive Dirac fermions induces an anomalous Hall effect, from which one can extract T_C through Arrott plots of the Hall resistances (Supplementary Fig. 10). The onset of the ferromagnetic order in the AFM/MTI bilayer is found to appear at a significantly higher temperature ($\sim$54 K) than the single MTI layer ($\sim$38 K) with the same Cr-doping concentration ($x = 0.16$). In the case of SL, T_C as a function of n is shown in Fig. 4c and the corresponding Hall resistance results are shown in Supplementary Fig. 10. It can be clearly seen that the anomalous Hall signal persists at up to $\sim$90 K with the help of the AFM layers. Additionally, we observe $\sim$90% spontaneous magnetization in the (AFM/MTI)$_{n=4}$ SL (Supplementary Fig. 11 and Supplementary Information part (g)), further demonstrating the nearly single domain nature[6] of the SL, which is in sharp contrast to the single MTI layer.

The effective long-range exchange coupling can be quantified by the exchange field, H_{EX}, extracted from the double-switching feature of the SLs. The values of H_{EX} are obtained from minor loop measurements[23–25] as shown in Fig. 2c and Supplementary Figs 12–16. The temperature-dependent H_{EX} of n-period SLs are summarized in Fig. 4. As shown in Fig. 4a, H_{EX} increases dramatically up to $\sim$50 mT at $T = 5$ K. As temperature increases, H_{EX} eventually vanishes at $\sim$90 K for $n = 10$. This result is consistent with the T_C values extracted from the transport measurements (Fig. 4c). The corresponding H_{EX} isotherms are shown in Fig. 4b for clarity. It should be highlighted that the coupling along the c-axis crosses many van der Waals gaps within MTI quintuple layers, showing a signature of long-range ferromagnetism[26–28]. In addition to H_{EX}, the enhancement in the magnetic order is also demonstrated by the increase in H_C. In Fig. 4e, H_C as a function of temperature is compared between SLs and isolated MTI thin films. For SLs, the maximum increase in H_C is roughly two orders of magnitude as compared to those of single layers of MTIs. In this measurement, single layers of MTIs do not show a distinct thickness-dependent H_C, implying a carrier-independent Van Vleck magnetism[29].

To further confirm that the long-range magnetic order is mediated by the AFM spin texture, Cr-doping concentration was varied in order to adjust the exchange coupling energy inside the MTI layers. In order to preserve the MTI surface spin tilting induced by the AFM layers, the internal exchange coupling within the MTI layer should be smaller than or comparable to the interfacial exchange. The increased concentration of Cr dopants reduces the average distance between the spins in the MTI layer, and thus increases the internal exchange energy. When the latter dominates, the surface spins in the MTI layers cannot be pinned by the spins in the AFM layer, such that the double-switching signature should vanish. Experimentally H_{EX} in the SLs decreases with increasing saturation magnetization M_s (corresponding to increasing Cr concentrations $x = 0.05$, 0.09, 0.13, 0.16 and 0.19) respectively, consistent with the expectation as discussed above. Although further increasing Cr concentration can further enhance the magnetic order in the MTI layer, the TI surface state becomes more massive and eventually loses its topological order[30]. This should be avoided in the study of TI surface states and their interplay with magnetic orders.

We have demonstrated intimate connections between heterostructure geometry and magnetic spin textures of the MTIs and AFMs. The AFM is shown to be an efficient interfacial exchange coupling mediator between the spins inside different MTI layers, which additionally allows a giant enhancement in magnetic ordering and a modification of the composite magnetic order. In particular,

our results revealed several advantages of AFM-based proximity-effect engineering over conventional FM-based systems, including longer-range interactions. This work unveils enormous opportunities for integrating and modifying topological surface states through coupling to AFM antiferromagnetic order, opening new avenues towards structural engineering of MTIs and showcasing the benefits of integrating MTIs with AFMs.

Methods

Methods and any associated references are available in the online version of the paper.

References

1. Chen, Y. L. et al. Massive Dirac fermion on the surface of a magnetically doped topological insulator. Science 329, 659–662 (2010).
2. Qi, X.-L., Hughes, T. L. & Zhang, S.-C. Topological field theory of time-reversal invariant insulators. Phys. Rev. B 78, 195424 (2008).
3. Yu, R. et al. Quantized anomalous Hall effect in magnetic topological insulators. Science 329, 61–64 (2010).
4. Li, R., Wang, J., Qi, X.-L. & Zhang, S.-C. Dynamical axion field in topological magnetic insulators. Nat. Phys. 6, 284–288 (2010).
5. Mahfouzi, F., Nagaosa, N. & Nikolic, B. K. Spin–orbit coupling induced spin-transfer torque and current polarization in topological-insulator/ferromagnet vertical heterostructures. Phys. Rev. Lett. 109, 166602 (2012).
6. Chang, C. Z. et al. High-precision realization of robust quantum anomalous Hall state in a hard ferromagnetic topological insulator. Nat. Mater. 14, 473–477 (2015).
7. Chang, C. Z. et al. Experimental observation of the quantum anomalous Hall effect in a magnetic topological insulator. Science 340, 167–170 (2013).
8. Kou, X. et al. Metal-to-insulator switching in quantum anomalous Hall states. Nat. Commun. 6, 8474 (2015).
9. Jiang, Z. et al. Independent tuning of electronic properties and induced ferromagnetism in topological insulators with heterostructure approach. Nano Lett. 15, 5835–5840 (2015).
10. Lang, M. et al. Proximity induced high-temperature magnetic order in topological insulator–ferrimagnetic insulator heterostructure. Nano Lett. 14, 3459–3465 (2014).
11. Wei, P. et al. Exchange-coupling-induced symmetry breaking in topological insulators. Phys. Rev. Lett. 110, 186807 (2013).
12. Yang, W. et al. Proximity effect between a topological insulator and a magnetic insulator with large perpendicular anisotropy. Appl. Phys. Lett. 105, 092411 (2014).
13. Katmis, F. et al. A high-temperature ferromagnetic topological insulating phase by proximity coupling. Nature 533, 513–516 (2016).
14. Takei, W. J., Cox, D. E. & Shirane, G. Magnetic structures in the MnSb–CrSb system. Phys. Rev. 129, 2008–2018 (1963).
15. Snow, A. I. Magnetic moment orientation and thermal expansion of antiferromagnetic CrSb. Rev. Mod. Phys. 25, 127 (1953).
16. Nogués, J. & Schuller, I. K. Exchange bias. J. Magn. Magn. Mater. 192, 203–232 (1999).
17. Shiratsuchi, Y. et al. Detection and in situ switching of unreversed interfacial antiferromagnetic spins in a perpendicular-exchange-biased system. Phys. Rev. Lett. 109, 077202 (2012).
18. Kirby, B. J. et al. Phase-sensitive specular neutron reflectometry for imaging the nanometer scale composition depth profile of thin-film materials. Curr. Opin. Colloid Interface 17, 44–53 (2012).
19. Borchers, J. A. et al. Long-range magnetic order in Fe3O4/NiO superlattices. Phys. Rev. B 51, 8276–8286 (1995).
20. Lenz, K., Zander, S. & Kuch, W. Magnetic proximity effects in antiferromagnet/ferromagnet bilayers: the impact on the Néel temperature. Phys. Rev. Lett. 98, 237201 (2007).
21. Manna, P. K. & Yusuf, S. M. Two interface effects: exchange bias and magnetic proximity. Phys. Rep. 535, 61–99 (2014).
22. Wu, X. W. & Chien, C. L. Exchange coupling in ferromagnet/antiferromagnet bilayers with comparable T_C and T_N. Phys. Rev. Lett. 81, 2795–2798 (1998).
23. Mauri, D., Siegmann, H. C., Bagus, P. S. & Kay, E. Simple model for thin ferromagnetic films exchange coupled to an antiferromagnetic substrate. J. Appl. Phys. 62, 3047–3049 (1987).
24. Liu, Z. Y. & Adenwalla, S. Oscillatory interlayer exchange coupling and its temperature dependence in [Pt/Co]3/NiO/[Co/Pt]3 multilayers with perpendicular anisotropy. Phys. Rev. Lett. 91, 037207 (2003).

25. Wilson, M. J. *et al*. Interlayer and interfacial exchange coupling in ferromagnetic metal/semiconductor heterostructures. *Phys. Rev. B* **81,** 045319 (2010).
26. Abanin, D. A. & Pesin, D. A. Ordering of magnetic impurities and tunable electronic properties of topological insulators. *Phys. Rev. Lett.* **106,** 136802 (2011).
27. Zhu, J. J., Yao, D. X., Zhang, S. C. & Chang, K. Electrically controllable surface magnetism on the surface of topological insulators. *Phys. Rev. Lett.* **106,** 097201 (2011).
28. Liu, Q., Liu, C. X., Xu, C., Qi, X. L. & Zhang, S. C. Magnetic impurities on the surface of a topological insulator. *Phys. Rev. Lett.* **102,** 156603 (2009).
29. Li, M. *et al*. Experimental verification of the van Vleck nature of long-range ferromagnetic order in the vanadium-doped three-dimensional topological insulator Sb_2Te_3. *Phys. Rev. Lett.* **114,** 146802 (2015).
30. Jiang, Y. *et al*. Mass acquisition of Dirac fermions in magnetically doped topological insulator Sb_2Te_3 films. *Phys. Rev. B* **92,** 195418 (2015).

Author contributions

Q.L.H., X.K. and K.L.W. conceived and designed the experiments. Q.L.H., L.P, X.C. and K.M. performed the sample growth and device fabrication. B.Z. and X.H. carried out the TEM experiments. All the authors contributed to the measurements and analyses. A.J.G., S.M.D., B.J.K., W.R.II and J.A.B. performed the neutron experiments and analyses. Q.L.H., X.K., A.J.G., G.Yin and K.L.W. wrote the manuscript with contributions from all the authors.

Additional information

Supplementary information is available in the online version of the paper. Reprints and permissions information is available online at www.nature.com/reprints. Correspondence and requests for materials should be addressed to Q.L.H. or K.L.W.

Competing financial interests

The authors declare no competing financial interests.

Methods

MBE growth of hybrid magnetic structures. All heterostructures discussed in this work were fabricated in an ultrahigh vacuum molecular beam epitaxy (MBE) system. All samples were fabricated on epi-ready semi-insulating GaAs(111)B substrates. Prior to sample growth, oxide-desorption processes were carried out at 580 °C for 30 min. The substrate temperature was reduced and maintained at 200 °C for the remainder of the fabrication process. High-purity Bi and Cr were evaporated from standard Knudsen cells, whereas Sb, Se and Te were evaporated by standard thermal cracker cells. Real-time reflection high-energy electron diffraction (RHEED) was used to monitor all the growth cycles. For the growth of both Cr-doped $(Bi,Sb)_2Te_3$ and CrSb layers, RHEED patterns were optimized to very sharp, smooth, streaky patterns, while the intensity oscillations were used to calibrate growth rates. These growth rates were determined to be around 0.08 and 0.06 Å s^{-1} for Cr-doped $(Bi,Sb)_2Te_3$ and CrSb, respectively. Direct epitaxial growth of CrSb on the GaAs substrate results in a three-dimensional growth mode with low crystal quality. Thus, growth of a CrSb single layer is carried out on an undoped 2-nm-thick $(Bi,Sb)_2Te_3$ buffer layer on the GaAs substrate, dramatically improving the CrSb crystal quality. After film growth, 2 nm Al layers were evaporated on all the sample surfaces *in situ* at room temperature to prevent against contamination and oxidation.

Polarized neutron reflectometry. Polarized neutron reflectometry (PNR) measurements were carried out with the PBR beamline at the NIST Center for Neutron Research. Samples were field-cooled in an in-plane applied field of 700 mT to a temperature of 20 K. Measurements were performed in the specular reflection geometry, with the direction of wavevector transfer perpendicular to the superlattice surface. The neutron propagation direction was perpendicular to both the sample surface and the applied field direction. Based on magnetometry measurements showing in-plane magnetization saturation below the applied field of 700 mT, spin-flip scattering is not expected. Therefore, we measured the spin-up and spin-down reflectivities using full polarization analysis to ensure that the incident and scattered beams retained identical neutron polarization directions. We refer, therefore, only to the spin-up and spin-down non-spin-flip reflectivities, which are a function of the nuclear and magnetic scattering length density profiles. The magnetic profile was deduced through modelling of the data with the NIST Refl1d software package.

Neutron diffraction. Neutron diffraction measurements were performed on the BT-4 triple axis spectrometer and polarized beam measurements were performed on the BT-7 triple axis spectrometer with ^{3}He spin filters at the NIST Center for Neutron Research. Measurements were carried out in a temperature range of 5–300 K in a closed-cycle refrigerator. The incident and scattering neutron energy was 14.7 meV ($\lambda = 2.359$ Å), selected by pyrolitic graphite (PG) monochromator and analyzer crystals with multiple PG filters before and after the sample to eliminate higher-order neutrons. The Soller collimator configuration in downstream order was open-monochromator-40′-sample-40′-analyzer-open-detector. For polarized beam measurements, two different spin quantization axes were measured independently; the first with vertical spins out of the scattering plane (and therefore perpendicular to (0002)), and the second with spins polarized horizontally along the momentum transfer Q.

Magneto measurement. Hall bar devices with dimensions of 2 mm × 1 mm were fabricated for the transport measurements. Systematically altering experimental variables such as temperature, magnetic field, working frequency, and rotation angle, in addition to multiple lock-in amplifiers, and sourcemeters enable comprehensive and high-sensitivity transport measurements in all the devices[31].

References

31. Nguyen, V. D. *et al.* Detection of domain-wall position and magnetization reversal in nanostructures using the magnon contribution to the resistivity. *Phys. Rev. Lett.* **107,** 136605 (2011).